



OPEN

Using deep learning and molecular dynamics simulations to unravel the regulation mechanism of peptides as noncompetitive inhibitor of xanthine oxidase

Yi He^{1,4}, Kaifeng Liu^{1,4}, Fuyan Cao^{1,4}, Renxiu Song¹, Jianxuan Liu², Yinghua Zhang²✉, Wannan Li³✉ & Weiwei Han¹✉

Xanthine oxidase (XO) is a crucial enzyme in the development of hyperuricemia and gout. This study focuses on LWM and ALPM, two food-derived inhibitors of XO. We used molecular docking to obtain three systems and then conducted 200 ns molecular dynamics simulations for the Apo, LWM, and ALPM systems. The results reveal a stronger binding affinity of the LWM peptide to XO, potentially due to increased hydrogen bond formation. Notable changes were observed in the XO tunnel upon inhibitor binding, particularly with LWM, which showed a thinner, longer, and more twisted configuration compared to ALPM. The study highlights the importance of residue F914 in the allosteric pathway. Methodologically, we utilized the perturbed response scan (PRS) based on Python, enhancing tools for MD analysis. These findings deepen our understanding of food-derived anti-XO inhibitors and could inform the development of food-based therapeutics for reducing uric acid levels with minimal side effects.

Gout, a significant health threat, arises from excessive intake of purine-rich foods and alcohol, leading to uric acid accumulation in body tissues^{1,2}. Hyperuricemia, gout's precursor, is linked to cardiovascular, kidney, and metabolic disorders³. Xanthine oxidase (XO) plays a crucial role in this process, also contributing to oxidative stress-related diseases⁴⁻⁶. Current XO-targeting drugs like allopurinol and febuxostat have safety concerns⁷. Therefore, finding safe, effective natural XO inhibitors is vital⁸. Recent research has identified XO inhibitory peptides from foods like walnut, rice, tuna and bonito have been reported⁹⁻¹². Specifically, two new peptides, ALPM and LWM, derived from whey protein isolate (WPI) hydrolysates, have shown promise, with IC₅₀ values of 7.23 ± 0.22 and 5.01 ± 0.31 mM, respectively. Both exhibit non-competitive inhibition modes¹³. Allosteric inhibition is often more specific than orthosteric or competitive inhibition at the active site, theoretically reducing off-target interactions that are commonly associated with side effects. Peptides especially Whey-derived-peptides can be added into dairy product such as yogurt and milk powder, so that we can develop food with anti-gout property.

It is an interesting and important proposition to explore how binding events of non-competitive inhibitors affect the interactions of protein active pockets with substrates¹⁴⁻¹⁶. Computational approaches for the analysis of allosteric coupling provide affordable opportunities to predict mutations or small molecule combinations to affect the active center^{17,18}. Gaussian Network Models (GNM)¹⁹ and Anisotropic Network Models (ANM)²⁰ are widely utilized to represent and analyze Elastic Network Models (ENM)²¹. For predicting key residues in allosteric transitions, Perturbation Response Scanning (PRS)²²⁻²⁴ applies isotropic perturbations to each residue, employing Linear Response Theory (LRT)²⁵ to derive the fluctuation response profile of the entire network. Additionally, Constraint Network Analysis (CNA)²⁶ is employed on network ensembles from MD trajectories to calculate neighbor stability maps and evaluate long-range effects of dynamic allostery using rigidity theory. The advent of deep learning, particularly the unsupervised Neural Relational Inference (NRI)²⁷ model, offers

¹Key Laboratory for Molecular Enzymology and Engineering of Ministry of Education, School of Life Sciences, Jilin University, Qianjin Road 2699, Changchun 130012, China. ²Jilin Academy of Chinese Medicine Sciences, Chuangju Road 155, Changchun 130012, China. ³Edmond H. Fischer Signal Transduction Laboratory, School of Life Sciences, Jilin University, Qianjin Road 2699, Changchun 130012, China. ⁴These authors contributed equally: Yi He, Kaifeng Liu and Fuyan Cao. ✉email: zhangyinghua0214@126.com; liwannan@jlu.edu.cn; weiweihan@jlu.edu.cn

novel approaches in studying allosteric regulations. The NRI-MD²⁸ model, an adaptation of the NRI algorithm, excels in identifying distal protein residue interactions.

Molecular dynamics simulation is a strong method to investigate conformational changes of proteins, protein folding, protein–ligand binding, etc.^{29,30} In this study, we conducted 200 ns classical molecular dynamics simulation after global molecular docking, we also utilized deep learning method NRI-MD²⁸ to reveal allosteric pathways, and explored the specific mechanism of non-competitive inhibition of XO by two different peptide inhibitors, including differences in peptide structure and different effects on protein conformations. This study may provide clues for the rational design of peptide inhibitors for XO.

Materials and methods

System preparation

Comparative modeling of XO's 3D structure and incorporation of the missing residues were performed on the basis of bovine milk xanthine oxidoreductase (PDB ID: 3BDJ)³¹ (1442 residues) using MODELER 10.1^{32,33}, the domains and the structure were shown in Fig. 1A. The two peptides (ALPM and LWM) were constructed using Pymol. Next, we used Gaussian 16³⁴ to optimize the structures of the two dipeptides at the level of B3LYP/6-31G* in order to obtain the optimal conformations for subsequent molecular docking. We utilized Autodock Vina 4.2³⁵ for global molecular docking^{36–38}, since both inhibitors are non-competitive inhibitors³⁹, docking poses to active sites were ignored, and the lowest energy structure was selected as the initial structures for MD simulations, which can be seen in Fig. 1B and C. The Amber FF14SB force field^{40,41} were used for proteins, and the TIP3P water model^{42,43} was added for these systems. The parameterization protocol applied for the flavin adenine dinucleotide (FAD), molybdenum cofactor (MOA) and Fe₂S₂ cluster (FES) have been described previously^{44,45}.

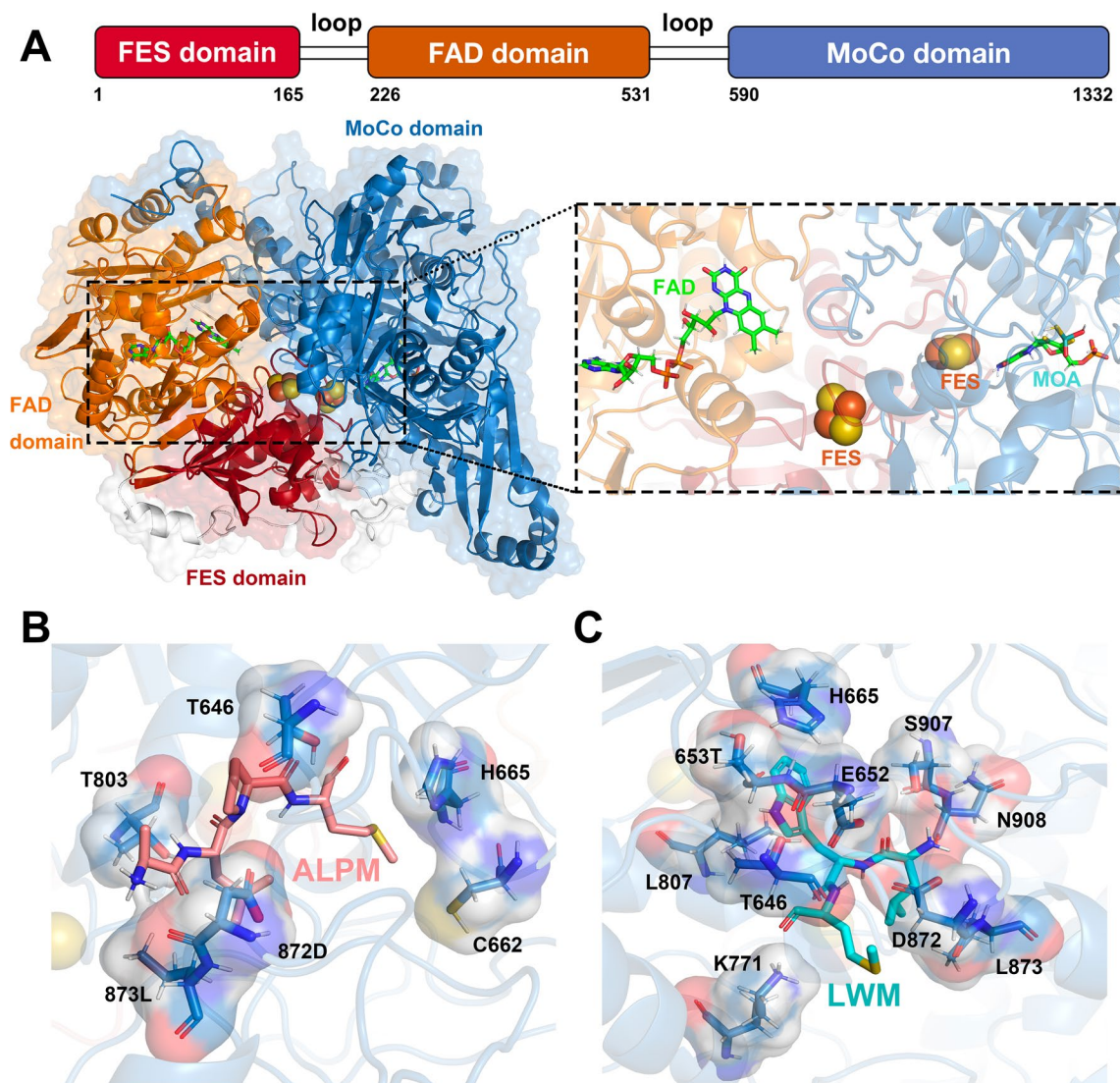


Figure 1. (A) 3D structure of one subunit of XO, the close-up represents the XO's active region. (B) Binding pocket of ALPM. (C) Binding pocket of LWM.

To avoid edge effects, periodic boundary conditions were given to the system during the simulation duration. The distance between the solute surface and the box was set to 12 Å. Since the charge in the initial reaction system is not zero, it was necessary to add Cl⁻ to the system in the initial stage of reaction simulation.

Systems under study were designated as follows: ALPM (Ala–Leu–Pro–Met) for XO–ALPM, LWM (Leu–Trp–Met) for XO–LWM, and Apo for XO without inhibitors.

Molecular dynamics simulations

In our experiment, PMEMD.CUDA module⁴⁶ of Amber 22 software⁴⁷ was used to simulate the systems with 200 ns molecular dynamics simulations. All the bonds involving hydrogen atoms were constrained using the SHAKE algorithm⁴⁸. The particle mesh Ewald (PME) algorithm⁴⁹ was used to handle non-bonded electrostatic interactions, and the cut off was set to 8 Å.

After the systems were constructed, energy minimization for the three systems was carried out to eliminate atomic collisions in the initial structures. The whole process is divided into two parts, the steepest descent and the conjugate gradient method with 500 steps respectively. The initial structures of the systems were stable after energy minimization, and the reaction time of 50 ps was used to raise the temperature of the simulated reaction from 0 to 300 K. After heating, the simulated systems were then treated with 50 ps of reaction time for density equilibration. Finally, the simulated systems were equilibrated with a constant pressure operation under NPT ensemble, with a constant pressure balance of 500 ps at 300 K. Constant pressure equilibration was the last step of system equilibration. After all, the thermodynamic parameters were stabilized, and then 200 ns molecular dynamics simulations were carried out for the three simulated systems. And the experimental data collection interval was set at 1 fs for each system. The entire simulation used a time step of 2 fs, and a Langevin thermostat⁵⁰ with a collision frequency of 1 ps. The storage interval is 2 ps/interval and the total record structure is 2000 frames. The data were kept for further study and analysis.

Trajectory analysis

The CPPTRAJ module of Amber22 was used for the trajectory analysis, which included calculations for the RMSD, RMSF, R_g , SASA, and hydrogen bond analysis⁵¹. K-means clustering was also performed utilizing CPPTRAJ, ten representative structures were obtained from each system. The tunnel analysis were obtained using CAVER 3.0⁵².

MM-PBSA calculation

The MM-PBSA method as applied to small molecule binding is an end-point method estimating the binding free-energy difference between the protein–ligand complex^{53–56}. The single-trajectory approach is favored for its straightforward implementation and cancellation of covalent energy errors as conformations for the complex and separated receptor and ligand are based on shared configurations from MD simulations.

MM-PBSA is often used in tandem with the closely related Molecular Mechanics Generalized Born Surface Area (MM-GBSA) approach as both utilize the same set of inputs for the prediction of binding free energies with continuum solvation^{57–59}:

$$\Delta G_{\text{bind}} = G_{\text{complex}} - G_{\text{receptor}} - G_{\text{ligand}} \quad (1)$$

$$\Delta G_{\text{bind}} = \Delta H - T\Delta S \quad (2)$$

$$\Delta H = \Delta E_{\text{ele}} + \Delta E_{\text{vdW}} + \Delta G_{\text{PB}} + \Delta G_{\text{SA}} \quad (3)$$

$$\Delta G_{\text{SA}} = \gamma \Delta \text{SASA} + \beta \quad (4)$$

In our calculation, for the ionic strength, a value of 0.1 M was used, and for the dielectric constants of the solvent and the solute, values of 80.0 and 1.0 were used, respectively^{60,61}, 500 snapshots were extracted from the final trajectory for MM/PBSA calculation.

Allosteric path analysis

The work flow of allosteric path analysis was shown in Fig. 2. NRI-MD²⁸ (<https://github.com/juexinwang/NRI-MD>) was used to infer residue-level and domain-level interaction, and then used Dijkstra algorithm to list shortest allosteric path. NRI-MD inferred the degree of interaction between residues from the simulated trajectory of the protein through unsupervised learning, which is achieved by obtaining hidden variables in the process of trajectory reconstruction. These latent variables are the low-dimensional spatiotemporal characteristic abstracted from protein trajectories, which can well reflect the internal relationship between residues. By accumulating the residue interactions within the domain, the domain-domain interaction profile of the protein can be obtained. Since NRI-MD's current algorithm cannot support protein trajectories with more than 150 residues, we sampled XO's protein every 10 residues, and the original 1332 residue-sized protein was compressed to 134 residues. Next we divided 2000-frames of XO's trajectory into train, validate, and test sets at intervals of 30, 40, and 50 frames, respectively. The default encoder and decoder of the model are multilayer perceptron (MLP) and recurrent neural networks (RNN) were used, respectively.

We used first and half frame of all-atomic trajectory as an ensemble of networks for thermal unfolding simulation to produce a contact matrix by CNA, and then use Bio3D⁶² cnapath to generate corresponding allosteric

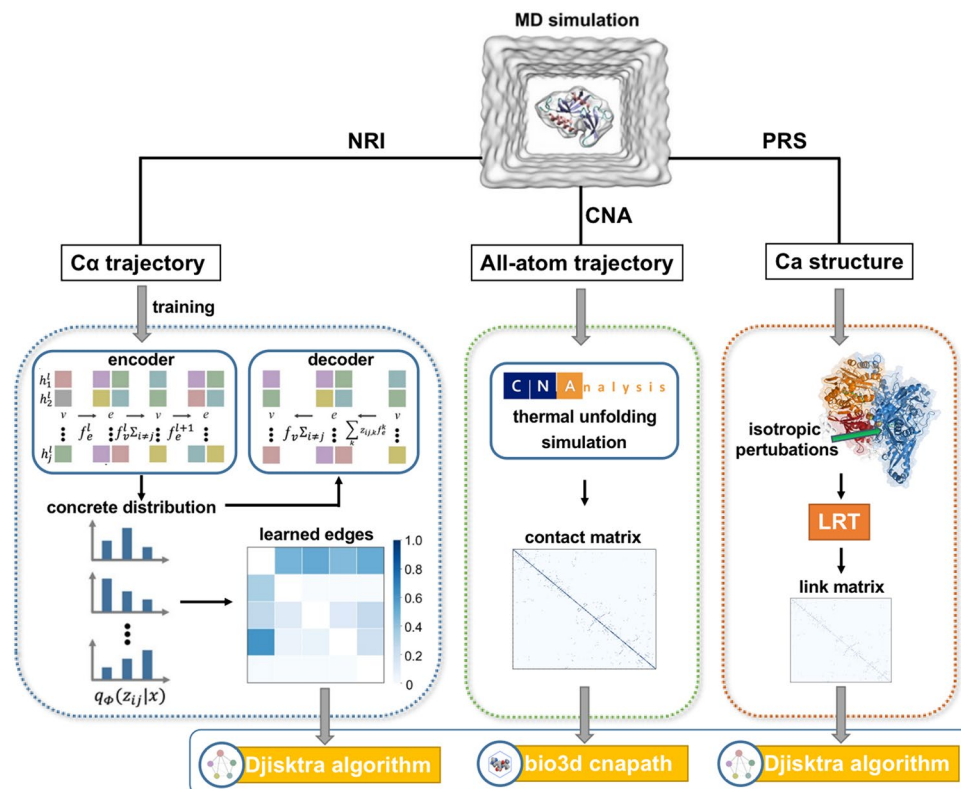


Figure 2. The work flow of allosteric path analysis.

paths. CNA simulates the unfolding process of the protein by removing the covalent bonds in the protein, thereby obtaining the residue contacts in the protein.

Perturbed response Scan (PRS) excels in identifying residues imperative for conformational shifts and inter-residue communication. We implemented PRS based on Python rather than prody, we also added the ability to point out key residues and visualize them. In PRS, we use the Fibonacci algorithm to generate 100 unit forces uniformly dividing the three-dimensional space and apply them to the disturbance sites to ensure isotropic perturbations, and then use LRT to screen the associated residues, and finally use the Dijkstra's algorithm to generate the shortest paths.

Results and discussion

The binding mode of inhibitors to XO

The binding poses of ALPM and LWM were determined by molecular docking, shown in Fig. 1B and C. The binding force between ALPM and XO consists of Van der Waals forces provided by E652, T653, V654, V663, G664, I666, K771, F775, K807, L834, N869, S907, N908, T909, hydrogen bonds provided by T646, T803, R804, D872, alkyl and pi-alkyl forces by C662, H665, L873 and charge attraction provided by D872. While the binding force between LWM and XO consists of Van der Waals forces provided by L648, V654, I666, F775, T803, R804, H849, E868, N869, N908, T909, A910, hydrogen bonds provided by T646, E652, T653, K771, D872, S907, alkyl and pi-alkyl forces by H665, L807, L873 and charge attraction provided by E652.

Structural stability and dynamics properties of the four systems

Following the generation of MD trajectories, the stability of simulations was assessed by calculating the root mean square deviation (RMSD) of CA atoms (as shown in Fig. 3A and B). After approximately 70 ns of simulations, equilibrium was reached in the RMSD of all three MD trajectories, suggesting the stability of all systems. However, in the the ALPM system, a broader attribution was noted, hinting at its lower stability in comparison to the other systems and more significant structural changes. Additionally, the minor mean RMSD values under 3 Å indicated no significant conformational changes in these systems. In summary, the equilibrated 200 ns trajectories were deemed suitable for further analysis.

The R_g (radius of gyration) value, an indicator of the overall size and compactness of the protein conformation, was found to be higher for the ALPM system post 150 ns compared to the other systems. This suggested a larger volume for the ALPM in comparison to the other complexes (as shown in Fig. 3C and D). Furthermore, the broader attribution in the ALPM system indicated its lower stability compared to the other systems.

The solvent-accessible surface area (SASA) is used to estimate the number of residues present in the surface regions of the protein and the number of residues that are in the hydrophobic core, which are buried. As shown

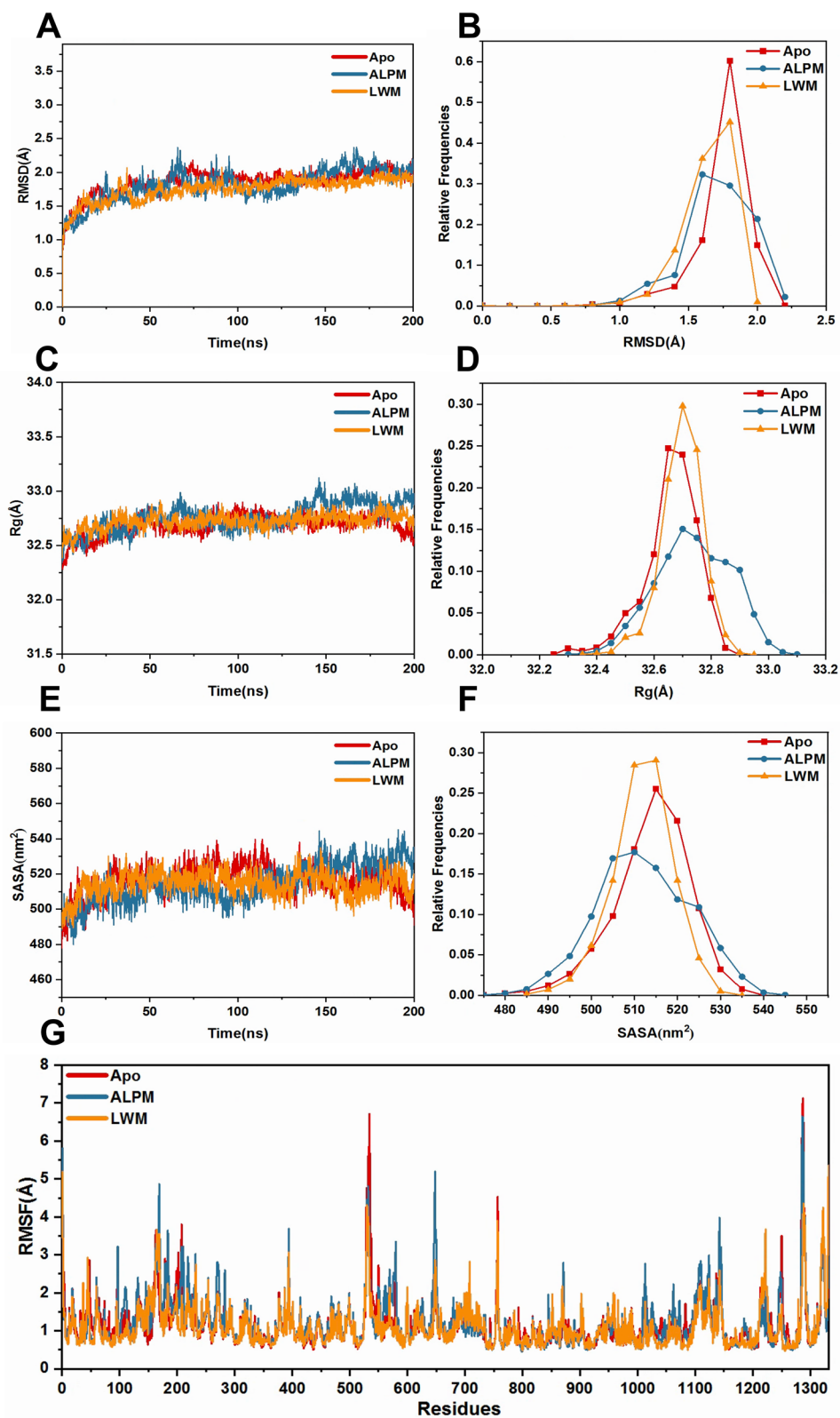


Figure 3. Analysis of structure stability. (A) The temporal evolution of the RMSDs from their initial structure of the three systems. (B) Relative Frequencies of RMSDs. (C) Radius of gyration over 200 ns MD for the three systems. (D) Relative Frequencies of radius gyration. (E) SASA over 200 ns MD. (F) Relative Frequencies of SASA. (G) The RMSFs of the CA atoms.

in Fig. 3E and F, SASA values was also found to be higher for the ALPM system post 150 ns in comparison to the other systems. Further more, the distribution of SASA in ALPM systems was also broader than that in Apo and LWM systems, which consistent with that of the R_g values.

Then we calculated RMSF values of CA atoms for the three systems to investigate stability. The results of RMSF were shown in Fig. 3G. LWM exhibited a lower RMSF than both Apo and ALPM, indicating better rigidity of XO after binding with LWM peptide. Also, reducing protein flexibility may be one reason why LWM peptide has better inhibitory activity than ALPM peptide.

Tunnel analysis

The tunnel is the access of the substrate to the catalytic site. Here, we used the F914, R880, E802 and E1261 residues to locate the active site for tunneling analysis of representative conformations of the three systems obtained by clustering. From the results shown in Fig. 4 and Table 1.

We can find that the tunnels became longer and narrower after combination of both inhibitors, with LWM of 12.18 Å, being longer and more tortuous than ALPM and Apo. Such a change is unfavorable for substrate to entry and may be the mechanism by which these two inhibitors are able to non-competitively inhibit XO.

Analysis of the interaction between protein and inhibitors

The results of MM-PBSA were shown in Table 2. The binding free energy of ALPM was -13.89 ± 1.02 kJ/mol, while the binding free energy of LWM was -35.54 ± 0.95 kJ/mol, the binding free energy was lower, indicated a better affinity.

We also analyzed hydrogen bonds, shown in Fig. 5. The analysis showed that the more hydrogen bonds were formed between protein and inhibitor in LWM system during 200 ns simulation than ALPM system. This provided a stronger binding force for LWM peptide.

Allosteric path analysis

To explore how binding events of the two non-competitive inhibitors affect the protein active pockets, and how they differ, we utilized multiple methods including deep learning. NRI-MD was used to inferred residue-level (Fig. 6) and domain-level (Fig. 7) interaction.

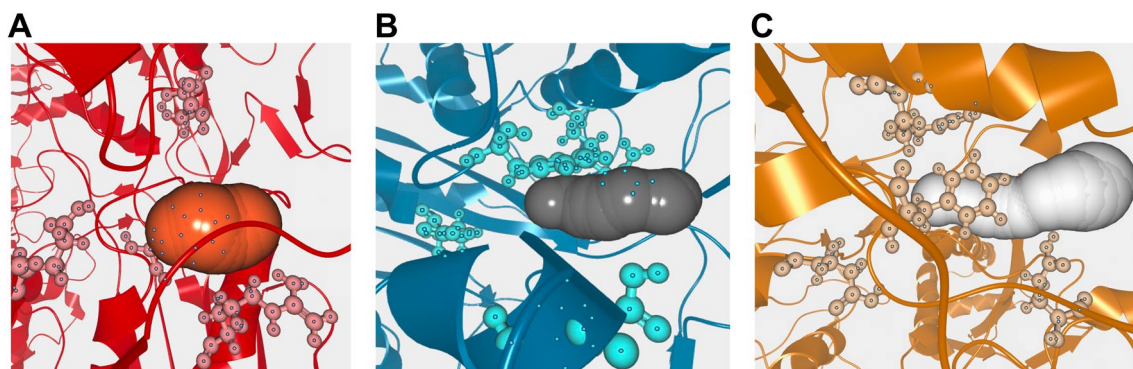


Figure 4. Representation of tunnels. (A) Apo. (B) ALPM. (C) LWM.

System	Bottleneck radius(Å)	Tunnel length(Å)
Apo	2.10	3.85
ALPM	1.77	7.88
LWM	1.76	12.18

Table 1. The result of tunnels analysis for three systems.

System	ALPM	LWM
ΔE_{vdw}	-30.81 ± 1.49	-40.52 ± 0.71
ΔE_{ele}	-198.46 ± 10.67	-302.56 ± 4.49
ΔG_{gas}	-229.27 ± 11.95	-338.11 ± 5.10
ΔG_{solv}	215.38 ± 11.18	302.56 ± 4.49
ΔG_{total}	-13.89 ± 1.02	-35.54 ± 0.95

Table 2. The results of MM-PBSA.

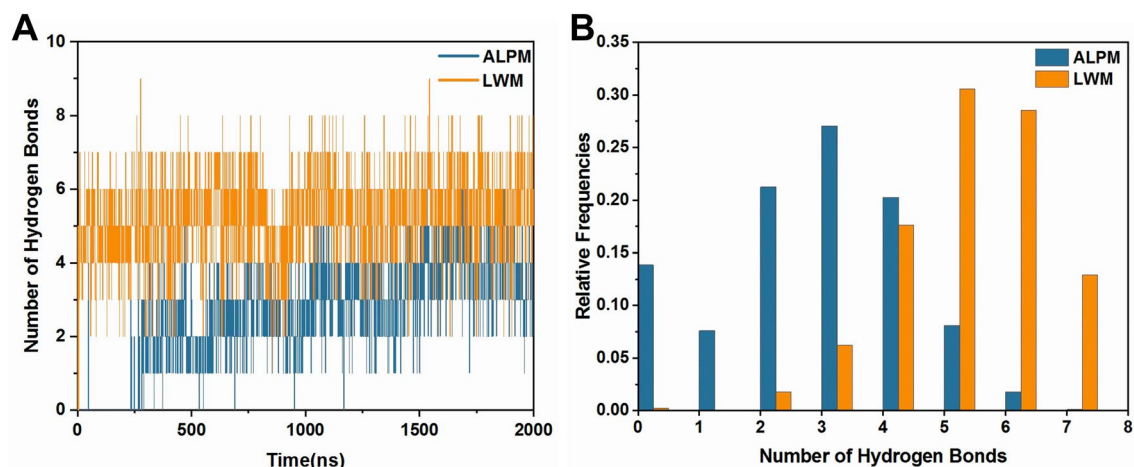


Figure 5. Analysis of hydrogen bonds. (A) Numbers of hydrogen bonds between receptor and inhibitors in the ALPM and LWM systems. (B) Frequency distribution of hydrogen bond numbers.

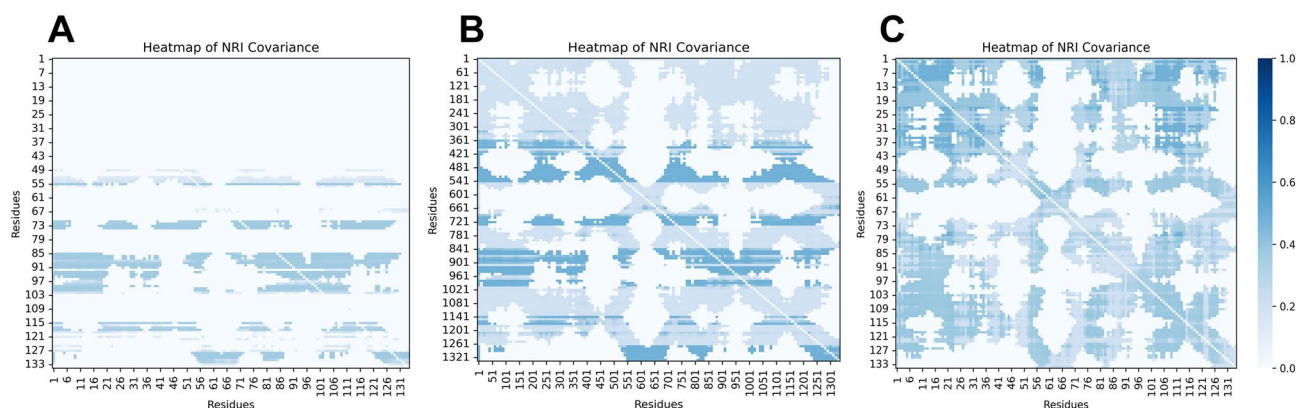


Figure 6. Heatmap of NRI covariance. (A) Apo. (B) ALPM. (C) LWM.

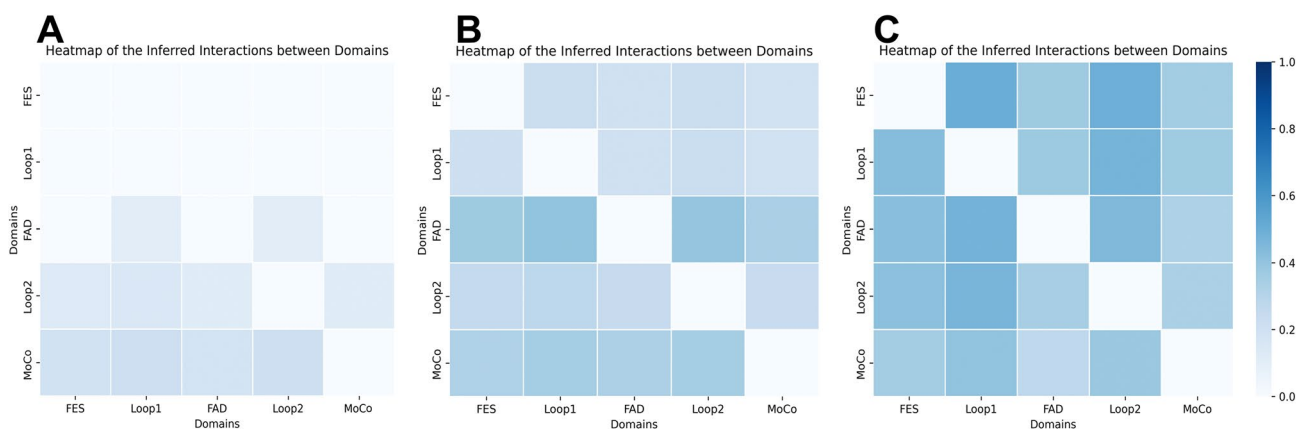


Figure 7. Heatmap of the inferred interactions between covariance. (A) Apo. (B) ALPM. (C) LWM.

In the LWM system, the interaction between residues and that between domains was found to be the strongest, followed by the ALPM system, with the Apo system showing the least interaction. This suggested that the relatively looser conformation of the empty protein did not allow for significant internal interaction, whereas the internal interaction of the inhibited XO was enhanced with the increase in the inhibitory effect. In the empty protein state, domain interactions were predominantly concentrated between the loop2 and MoCo domains. The binding of the inhibitor, however, amplified interactions with the FES, Loop1, and FAD domains. This was consistent with the occurrence of allosteric binding or mutation in the NRI-MD article which increased interdomain

communication. Furthermore, in the NRI-MD study, the accumulation of residue-to-residue interactions was described as an indicator-free energy fraction. The change in free energy fraction, before and after allosterism, was found to be linearly related to the experimentally measured free energy. Therefore, the combination of LWM and ALPM increased the free energy of the system, rendering the system relatively more unstable.

Then, constraint network analysis (CNA) was used to calculate neighbor stability maps, shown in Fig. 8. The stability maps reflect the local stabilities of the residue-residue contacts. Similar CNA maps revealed that the change of the active site was not simply the result of the changes of a few residues, but the accumulation of small energy and conformational changes of multiple residues.

By applying isotropic perturbations to each residues, perturbation response scanning (PRS) were used to obtain the corresponding fluctuation response of the entire protein network. As can be seen in Fig. 9, the response to perturbation was stronger with LWM peptide inhibiting, while the response intensity decreased in ALPM and Apo. The results of the PRS were consistent with those of the NRI. This indicated that after the combination of the two allosteric inhibitors, the residues in the protein were more closely linked, which made the allosteric interaction affected the active center of the junction to achieve an inhibition effect.

Here, we generate allosteric paths using these three methods, and the path information is in the Table S1. Due to sampling was not precise enough, we did not plot the paths presented by NRI-MD and PRS, but picked the CNA results instead. The allosteric paths are shown in Fig. 10, the start nodes are orange, the middle nodes are white, and the end nodes are green. In Apo, the transfer path is relatively simple, and R804 and S914 are nodes through which multiple paths pass, which is more important. However, in ALPM, we can see relatively complicated and chaotic transmission paths, which may also lead to poor inhibition effect. Similarly, E802 and F914 show relatively important hub status. Finally, the path of LWM is clearly divided into two parts: the upper node is S907, and the lower node is T803, which converge to F914 and thus allosteric the active site.

F914 is an important conformational change transmission site since it was a most mediated site in the network of allosteric pathways from binding sites to active sites. Although F914 now has not been shown experimentally to be a key allosteric residue in other study about XO, but there were some works showed the prediction are consistent with the experiment. For example, Ohm (used perturbation propagation algorithm) predicted that R286 and E390 are the most critical residues in the Caspase-1 allosteric network, S332, S333, and S339 were the next most important residues that are in perfect accord with experimental results (mutated nine residues of Caspase-1 to test their roles in allosteric pathways)⁶³. And PRS predicted the allosteric pathways in PIN1⁶⁴. These successful examples proved that our reasoning has some reliability.

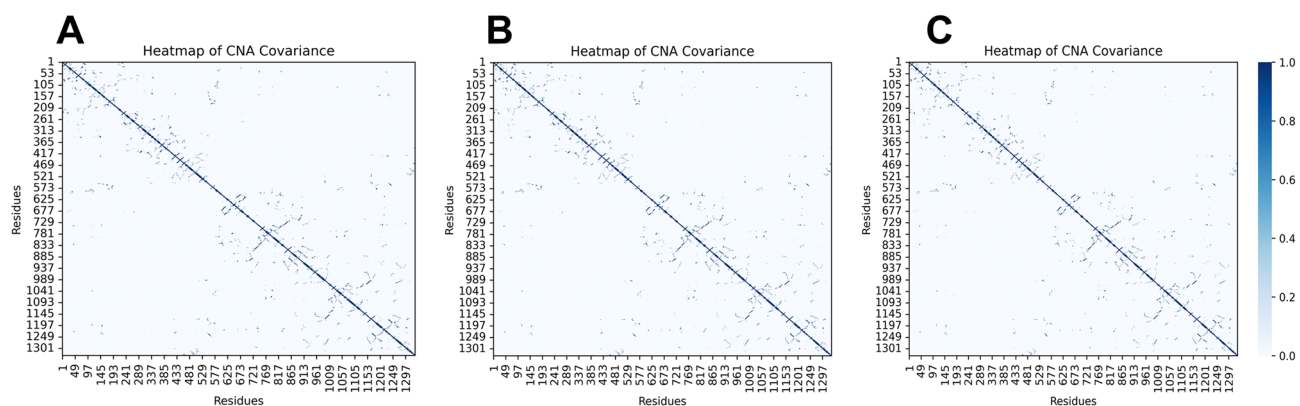


Figure 8. Heatmap of CNA covariance. (A) Apo. (B) ALPM. (C) LWM.

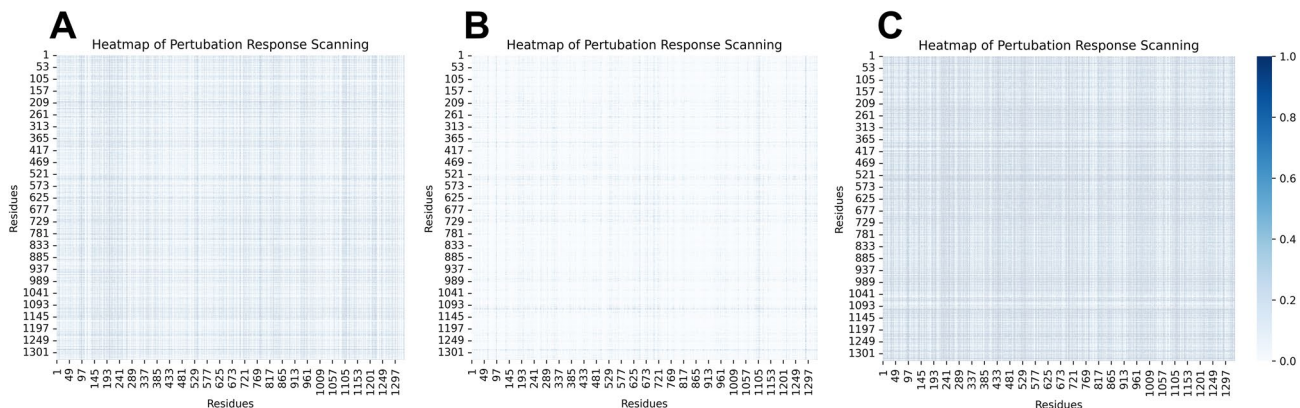


Figure 9. Heatmap of perturbation response scanning. (A) Apo. (B) ALPM. (C) LWM.

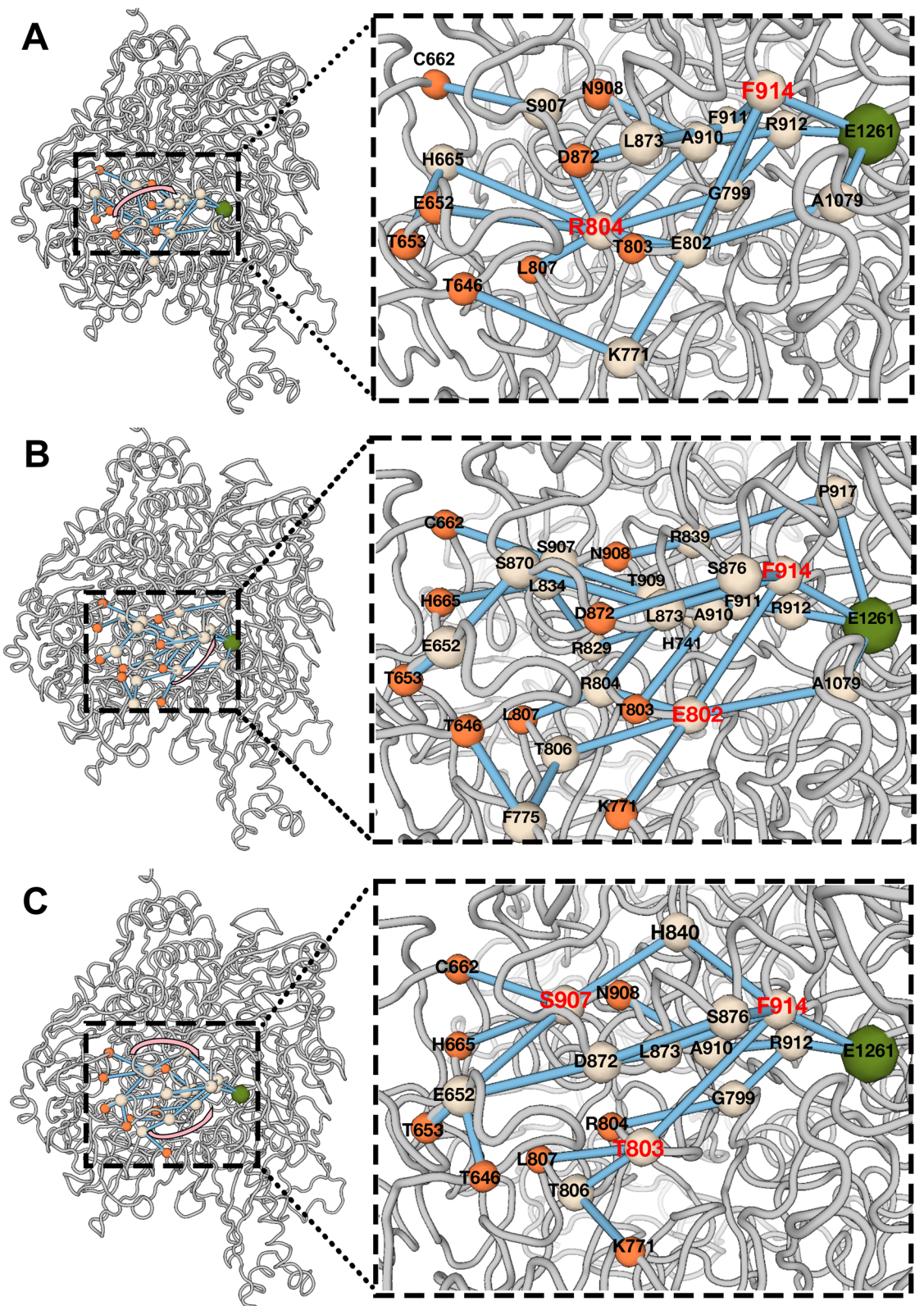


Figure 10. Conformational transition transduction pathways in proteins. The start nodes are orange, the middle nodes are white, and the end nodes are green. (A) Apo. (B) ALPM. (C) LWM.

Conclusions

In this study, we conducted 200 ns molecular dynamics simulations of Apo, LWM and ALPM systems and carried

out a variety of analyses. The results show that LWM peptide and XO have stronger binding ability, which may be related to more hydrogen bonds. After binding to the inhibitor, the XO tunnel deforms, while LWM is thinner, longer and more tortuous than ALPM. In addition, studies of allosteric pathways have found that F914 may be a key residue in the allosteric path. Our study will provide new insights into food-derived anti-XO inhibitors and may contribute to the development of food drugs that reduce uric acid without side effects.

Data availability

PRS is implemented based on Python, and the detailed code can be available in <https://github.com/heyigacu/PRS>.

Received: 24 October 2023; Accepted: 22 December 2023

Published online: 02 January 2024

References

- Saito, Y., Tanaka, A., Node, K. & Kobayashi, Y. Uric acid and cardiovascular disease: A clinical review. *J. Cardiol.* **78**(1), 51 (2021).
- Lin, A. Q. *et al.* Self-cascade uricase/catalase mimics alleviate acute gout. *Nano Lett.* **22**(1), 508 (2022).
- Han, T. J., Wang, M. Y., Li, W. C., An, M. X. & Fu, H. Z. Bmk9 and uricase nanoparticle complex for the treatment of gouty arthritis and uric acid nephropathy. *J. Biomed. Nanotechnol.* **17**(10), 2071 (2021).
- Cao, H., Hall, J. & Hille, R. Substrate orientation and specificity in xanthine oxidase: Crystal structures of the enzyme in complex with indole-3-acetaldehyde and Guanine. *Biochemistry* **53**(3), 533 (2014).
- Cao, H. N., Paufl, J. M. & Hille, R. X-ray crystal structure of a xanthine oxidase complex with the flavonoid inhibitor quercetin. *J. Nat. Prod.* **77**(7), 1693 (2014).
- Leigh, M., Raines, D. J., Castillo, C. E. & Duhme-Klair, A. K. Inhibition of xanthine oxidase by thiosemicarbazones, hydrazones and dithiocarbazates derived from hydroxy-substituted benzaldehydes. *ChemMedChem* **6**(6), 1107 (2011).
- Vasta, L. M., Zanetti, R. C., Parekh, D. S., Warwick, A. B. & Lieuw, K. A retrospective review of mercaptopurine metabolism reveals high rate of patients with suboptimal metabolites successfully corrected with allopurinol. *J. Pediatr. Hematol. Oncol.* **43**(7), E1003 (2021).
- Orhan, I. E. & Deniz, F. S. S. Natural products and extracts as xanthine oxidase inhibitors - A hope for gout disease?. *Curr. Pharm. Des.* **27**(2), 143 (2021).
- Li, Q. *et al.* Moderation of hyperuricemia in rats via consuming walnut protein hydrolysate diet and identification of new anti-hyperuricemic peptides. *Food Funct.* **9**(1), 107 (2018).
- Li, Y. *et al.* Anti-hyperuricemic peptides derived from bonito hydrolysates based on in vivo hyperuricemic model and in vitro xanthine oxidase inhibitory activity. *Peptides* **107**, 45 (2018).
- He, W. *et al.* In vivo anti-hyperuricemic and xanthine oxidase inhibitory properties of tuna protein hydrolysates and its isolated fractions. *Food Chem.* **272**, 453 (2019).
- Liu, N. *et al.* New rice-derived short peptide potentially alleviated hyperuricemia induced by potassium oxonate in rats. *J. Agric. Food Chem.* **67**(1), 220 (2019).
- Qi, X. *et al.* Novel xanthine oxidase inhibitory peptides derived from whey protein: Identification, in vitro inhibition mechanism and in vivo activity validation. *Bioorg. Chem.* **128**, 106097 (2022).
- Yasar, Ü., Gönül, I., Türkes, C., Demir, Y. & Beydemir, S. Transition-metal complexes of bidentate schiff-base ligands: In vitro and in silico evaluation as non-classical carbonic anhydrase and potential acetylcholinesterase inhibitors. *Chemistryselect* **6**(29), 7278 (2021).
- Güleç, Ö. *et al.* Cytotoxic effect, enzyme inhibition, and in silico studies of some novel N-substituted sulfonyl amides incorporating 1,3,4-oxadiazol structural motif. *Mol. Divers.* **26**(5), 2825 (2022).
- Sever, B. *et al.* Design, synthesis, in vitro and in silico investigation of aldose reductase inhibitory effects of new thiazole-based compounds. *Bioorg. Chem.* **102**, 104110 (2020).
- Demir, Y., Ceylan, H., Türkes, C. & Beydemir, S. Molecular docking and inhibition studies of vulpinic, carnosic and usnic acids on polyol pathway enzymes. *J. Biomol. Struct. Dyn.* **40**(22), 12008 (2022).
- Osmaniye, D. *et al.* Design, synthesis, and biological activity of novel dithiocarbamate-methylsulfonyl hybrids as carbonic anhydrase inhibitors. *Archiv Der Pharmazie* **355**(8), 2200132 (2022).
- Doruker, P., Atilgan, A. R. & Bahar, I. Dynamics of proteins predicted by molecular dynamics simulations and analytical approaches: Application to α -amylase inhibitor. *Proteins-Struct. Funct. Genet.* **40**(3), 512 (2000).
- Atilgan, A. R. *et al.* Anisotropy of fluctuation dynamics of proteins with an elastic network model. *Biophys. J.* **80**(1), 505 (2001).
- Tirion, M. M. Large amplitude elastic motions in proteins from a single-parameter, atomic analysis. *Phys. Rev. Lett.* **77**(9), 1905 (1996).
- Atilgan, C. & Atilgan, A. R. Perturbation-response scanning reveals ligand entry-exit mechanisms of ferric binding protein. *PLoS Comput. Biol.* **5**(10), e1000544 (2009).
- Atilgan, C., Gerek, Z. N., Ozkan, S. B. & Atilgan, A. R. Manipulation of conformational change in proteins by single-residue perturbations. *Biophys. J.* **99**(3), 933 (2010).
- Gerek, Z. N. & Ozkan, S. B. Change in allosteric network affects binding affinities of PDZ domains: Analysis through perturbation response scanning. *PLoS Comput. Biol.* **7**(10), e1002154 (2011).
- Ikeguchi, M., Ueno, J., Sato, M. & Kidera, A. Protein structural change upon ligand binding: Linear response theory. *Phys. Rev. Lett.* **94**(7), 078102 (2005).
- Pfleger, C. *et al.* Ensemble- and rigidity theory-based perturbation approach to analyze dynamic allostery. *J. Chem. Theory Comput.* **13**(12), 6343 (2017).
- Kipf, T., Fetaya, E., Wang, K. C., Welling, M., Zemel, R. *35th International Conference on Machine Learning (ICML)*, Stockholm, Sweden, (2018).
- Zhu, J., Wang, J., Han, W. & Xu, D. Neural relational inference to learn long-range allosteric interactions in proteins from molecular dynamics simulations. *Nat. Commun.* **13**(1), 1661 (2022).
- Poyraz, S. *et al.* Design, synthesis, biological evaluation and docking analysis of pyrrolidine-benzenesulfonamides as carbonic anhydrase or acetylcholinesterase inhibitors and antimicrobial agents. *J. Biomol. Struct. Dyn.* <https://doi.org/10.1080/07391102.2023.2214224> (2023).
- Güleç, Ö. *et al.* Novel beta-lactam substituted benzenesulfonamides: In vitro enzyme inhibition, cytotoxic activity and in silico interactions. *J. Biomol. Struct. Dyn.* <https://doi.org/10.1080/07391102.2023.2240889> (2023).
- Okamoto, K., Eger, B. T., Nishino, T., Pai, E. F. & Nishino, T. Mechanism of inhibition of xanthine oxidoreductase by allopurinol: Crystal structure of reduced bovine milk xanthine oxidoreductase bound with oxipurinol. *Nucleosides Nucleotides Nucl. Acids* **27**(6), 888 (2008).
- Eswar, N., Eramian, D., Webb, B., Shen, M.-Y. & Sali, A. Protein structure modeling with Modeller. *Methods Mol. Biol.* **426**, 145 (2008).

33. Webb, B. & Sali, A. Comparative protein structure modeling using modeller. *Curr. Protoc. Bioinform.* **54**, 5–6 (2016).
34. Frisch, M. J., Trucks G. W., Schlegel, H. B. *et al.* *Gaussian 09, Revision, A.02.* (Gaussian, Inc., Wallingford, 2009).
35. Eberhardt, J., Santos-Martins, D., Tillack, A. F. & Forli, S. AutoDock Vina 1.2.0: New docking methods, expanded force field, and python bindings. *J. Chem. Inf. Model.* **61**(8), 3891 (2021).
36. Hamide, M. *et al.* Pentafluorobenzyl-substituted benzimidazolium salts: Synthesis, characterization, crystal structures, computational studies and inhibitory properties of some metabolic enzymes. *J. Mol. Struct.* **1265**, 133266 (2022).
37. Knabe, J. & Holtje, H. D. Dihydroisoquinoline rearrangement. 12. Studies on the value range. *Archiv der Pharmazie und Berichte der Deutschen Pharmazeutischen Gesellschaft* **303**(5), 404 (1970).
38. Rehse, K. & Baselt, T. New 2-Amino-thiazole-4-acetamides with antiplatelet activity. *Archiv Der Pharmazie* **341**(10), 645 (2008).
39. Zhou, S., Huang, G. & Chen, G. Extraction, structural analysis, derivatization and antioxidant activity of polysaccharide from Chinese yam. *Food Chem.* **361**, 130089 (2021).
40. Maier, J. A. *et al.* ff14SB: Improving the accuracy of protein side chain and backbone parameters from ff99SB. *J. Chem. Theory Comput.* **11**(8), 3696 (2015).
41. Weber, O. C. & Uversky, V. N. How accurate are your simulations? Effects of confined aqueous volume and AMBER FF99SB and CHARMM22/CMAP force field parameters on structural ensembles of intrinsically disordered proteins: Amyloid- β (42) in water. *Intrinsically Disord. Proteins* **5**(1), e1377813 (2017).
42. Pathak, A. K. & Bandyopadhyay, T. Temperature induced dynamical transition of biomolecules in polarizable and nonpolarizable TIP3P water. *J. Chem. Theory Comput.* **15**(4), 2706 (2019).
43. Sattelle, B. M. & Almond, A. Less is more when simulating unsulfated glycosaminoglycan 3D-structure: comparison of GLY-CAM06/TIP3P, PM3-CARB1/TIP3P, and SCC-DFTB-D/TIP3P predictions with experiment. *J. Comput. Chem.* **31**(16), 2932 (2010).
44. Maghsoud, Y., Dong, C. & Cisneros, G. A. Investigation of the inhibition mechanism of xanthine oxidoreductase by oxipurinol: A computational study. *J. Chem. Inf. Model.* **63**(13), 4190 (2023).
45. Maghsoud, Y., Dong, C. & Cisneros, G. A. Computational characterization of the inhibition mechanism of xanthine oxidoreductase by tiropoxostat. *ACS Catal.* **13**(9), 6023 (2023).
46. Salomon-Ferrer, R., Götz, A. W., Poole, D., Le Grand, S. & Walker, R. C. Routine microsecond molecular dynamics simulations with AMBER on GPUs. 2. Explicit solvent particle mesh Ewald. *J. Chem. Theory Comput.* **9**(9), 3878 (2013).
47. Case, D. A. *AMBER* (University of California, San Francisco, 2016).
48. Hopkins, C. W., Le Grand, S., Walker, R. C. & Roitberg, A. E. Long-time-step molecular dynamics through hydrogen mass repartitioning. *J. Chem. Theory Comput.* **11**(4), 1864 (2015).
49. Darden, T., York, D. & Pedersen, L. Particle mesh Ewald: An N-log(N) method for Ewald sums in large systems. *J. Chem. Phys.* **98**(12), 10089 (1993).
50. Davidchack, R. L., Handel, R. & Tretyakov, M. V. Langevin thermostat for rigid body dynamics. *J. Chem. Phys.* **130**(23), 234101 (2009).
51. Roe, D. R. & Cheatham, T. E. PTRAJ and CPPTRAJ: Software for processing and analysis of molecular dynamics trajectory data. *J. Chem. Theory Comput.* **9**(7), 3084 (2013).
52. Chovancova, E. *et al.* CAVER 3.0: A tool for the analysis of transport pathways in dynamic protein structures. *PLoS Comput. Biol.* **8**(10), e1002708 (2012).
53. Sharp, K. A. & Honig, B. Electrostatic interactions in macromolecules: Theory and applications. *Annu. Rev. Biophys. Chem.* **19**, 301 (1990).
54. Cheatham, T. E., Srinivasan, J., Case, D. A. & Kollman, P. A. Molecular dynamics and continuum solvent studies of the stability of polyG-polyC and polyA-polyT DNA duplexes in solution. *J. Biomol. Struct. Dyn.* **16**(2), 265 (1998).
55. King, E., Aitchison, E., Li, H. & Luo, R. Recent developments in free energy calculations for drug discovery. *Front. Mol. Biosci.* **8**, 712085 (2021).
56. Wang, R. & Zheng, Q. Multiple molecular dynamics simulations and free-energy predictions uncover the susceptibility of variants of HIV-1 protease against inhibitors darunavir and KNI-1657. *Langmuir* **37**(49), 14407 (2021).
57. Case, D. A. *et al.* The Amber biomolecular simulation programs. *J. Comput. Chem.* **26**(16), 1668 (2005).
58. Chen, F. *et al.* Assessing the performance of the MM/PBSA and MM/GBSA methods. 6. Capability to predict protein-protein binding free energies and re-rank binding poses generated by protein-protein docking. *Phys. Chem. Chem. Phys.* **18**(32), 22129 (2016).
59. Wang, E. *et al.* Assessing the performance of the MM/PBSA and MM/GBSA methods. 10. Impacts of enhanced sampling and variable dielectric model on protein-protein Interactions. *Phys. Chem. Chem. Phys.* **21**(35), 18958 (2019).
60. Sun, H. *et al.* Assessing the performance of MM/PBSA and MM/GBSA methods. 5. Improved docking performance using high solute dielectric constant MM/GBSA and MM/PBSA rescoring. *Phys. Chem. Chem. Phys.* **16**(40), 22035 (2014).
61. Case, D. A. Normal mode analysis of protein dynamics. *Curr. Opin. Struct. Biol.* **4**(2), 285 (1994).
62. Grant, B. J., Rodrigues, A. P., ElSawy, K. M., McCammon, J. A. & Caves, L. S. Bio3d: An R package for the comparative analysis of protein structures. *Bioinformatics* **22**(21), 2695 (2006).
63. Wang, J. *et al.* Mapping allosteric communications within individual proteins. *Nat. Commun.* **11**(1), 3862 (2020).
64. Campitelli, P., Guo, J., Zhou, H.-X. & Ozkan, S. B. Hinge-shift mechanism modulates allosteric regulations in human Pin1. *J. Phys. Chem. B* **122**(21), 5623 (2018).

Author contributions

Conceptualization, W.H.; methodology, Y.H., K.L.; software, R.S.; validation, K.L., Y.H., J.L.; formal analysis, Y.H., R.S.; investigation, K.L., Y.H.; resources, Y.H.; data curation, K.L., F.C.; writing—original draft preparation, K.L., F.C.; writing—review and editing, Y.H.; visualization, K.L., Y.H.; supervision, W.H., Y.Z.; project administration, W.H., W.L.; funding acquisition, W.L. All authors have read and agreed to the published version of the manuscript. All authors reviewed the manuscript.

Funding

This research was funded by the Natural Science Foundation of Jilin Province of China (VDZJ202301ZYTS121 to Wannan Li).

Competing interests

The authors declare no competing interests.

Additional information

Supplementary Information The online version contains supplementary material available at <https://doi.org/10.1038/s41598-023-50686-0>.

Correspondence and requests for materials should be addressed to Y.Z., W.L. or W.H.

Reprints and permissions information is available at www.nature.com/reprints.

Publisher's note Springer Nature remains neutral with regard to jurisdictional claims in published maps and institutional affiliations.



Open Access This article is licensed under a Creative Commons Attribution 4.0 International License, which permits use, sharing, adaptation, distribution and reproduction in any medium or format, as long as you give appropriate credit to the original author(s) and the source, provide a link to the Creative Commons licence, and indicate if changes were made. The images or other third party material in this article are included in the article's Creative Commons licence, unless indicated otherwise in a credit line to the material. If material is not included in the article's Creative Commons licence and your intended use is not permitted by statutory regulation or exceeds the permitted use, you will need to obtain permission directly from the copyright holder. To view a copy of this licence, visit <http://creativecommons.org/licenses/by/4.0/>.

© The Author(s) 2024